A CFD Study of the Effects of Slots on Energy Harvesting from Flow-Induced Circular Cylinder Vibrations

A. Bekhti[†], M. Tata, D. Hamane and M. Maizi

Center for Renewable Energies Development, CDER, BP 62 Road of the Observatory, Bouzareah, 16340, Algiers, Algeria

†*Corresponding Author Email: a.bekhti@cder.dz*

ABSTRACT

In this paper, numerical investigations of the harnessed power from Flow-Induced Vibrations of a new modified circular cylinder are performed. The proposed cylinder modification consists in adding two slots located on the front surface of the cylinder, instead of the baseline configuration, usually applied, which consists of a Passive Turbulence Control in form two straight strips. The computations are based on the solution of the Unsteady Reynolds- Averaged Navier-Stokes equations (URANS) coupled with the dynamic equations system describing the cylinder motion, where turbulence is modeled using the two-equation SST $k - \omega$ model. The harvested and the harnessed powers are thereafter calculated according to the amplitude and the frequency of the cylinder oscillatory motion. The numerical results show that the slots lead to shift the flow separation point toward the leading edge, which involves higher hydrodynamic instabilities resulting in higher oscillations amplitudes, and thereby a significant enhancement of the harnessed power is noticed.

Keywords: CFD; Flow-Induced vibration; Elastically mounted cylinder; Turbulence; Energy harvesting.

NOMENCLATURE

A	oscillations amplitude	P_h	harnessed power
A*	dimensionless amplitude	P_m	mechanical power
ALE	Arbitrary Lagrangian Eulerian	PTC	Passive Turbulence Control
AoA	Angle of Attack	Re	Reynolds number
c	damping coefficient	T	one cycle oscillation time
c_h	damping coefficient for energy harnessing	t	time
CFD	Computational Fluid Dynamics	U_∞	far-field velocity
C_L	vertical force coefficient	y	vertical displacement
C_D	Drag force coefficient	$\dot{y}$	vertical velocity
D	cylinder diameter	$\ddot{y}$	vertical acceleration
DoF	Degree of Freedom	y^+	dimensionless wall distance
F	hydrodynamic force	δ_1, δ_2	PTC's dimensions
f	oscillations frequency	Δt	time step
f_{nw}	natural frequency in water	ε	turbulent dissipation rate
K	turbulent kinetic energy	ν	kinematic viscosity
k	stiffness	ρ	fluid density
m	mass	ω	turbulent specific dissipation rate
m_a	added mass	ζ	damping ratio

1. INTRODUCTION

Energy harvesting from an elastically-mounted rigid body has aroused increasing interest in recent years. Different techniques have been developed to harness energy resulting from bodies undergoing motion, which is otherwise considered harmful, with the risk of damaging structures. To convert the recovered mechanical energy to electricity, mostly three mechanisms are often used: piezoelectric electromagnetic and electrostatic transductions (Xie and Wang 2015). Harvesting energy systems were

mainly developed to operate in a marine environment and most of the oscillating bodies are bluff bodies, namely cylinders. Thereby, flow-induced vibrations of a circular cylinder for energy harvesting applications have been the subject of several publications and patents. Bernitsas *et al.* (2006) presented a device that converts ocean/river current energy to electricity. Their Vortex-Induced Vibration Aquatic Clean Energy (VIVACE) converter was patented in 2005 (Bernitsas and Raghavan 2005). The device consists of a rigid circular cylinder mounted on elastic springs and connected to a generator via a transmission mechanism (gear-belt). Subsequently, Chang *et al.* (2011) performed experimental tests on a circular cylinder with straight roughness strips placed on the cylinder surface. The width, the roughness, and the circumferential location of this passive turbulence control (PTC) were tested to highlight their influence on the harnessed power by the VIVACE converter. They showed that the amplitude reached three times the cylinder diameter during galloping and the vortex shedding increased to reach 10 vortices per oscillation cycle. These investigations were carried out at Reynolds numbers $3.0\,10^4 \leq Re \leq 1.2\,10^5$. For their part, Barrero-Gil *et al.* (2012) considered some parameters that control VIV of a spring-mounted circular cylinder, like the mass ratio (i.e. the ratio of the mean density of the body to the density of the surrounding fluid), the mechanical damping coefficient and the Reynolds number. Their parametric study revealed that the expected power efficiency is mainly influenced by the mass-damping parameter and the inflow velocity. Mehmood *et al.* (2013) performed numerical investigations on the energy harvesting from a circular cylinder undergoing vortex-induced vibrations attached to a piezoelectric transducer. The dynamic equations of the flow field were coupled to the equations that govern the dynamics of the cylinder and the generated voltage; the equations of the global system were solved simultaneously. The fluid equations were computed for Reynolds numbers in the range $96 \leq Re \leq 118$, and the load resistances considered were in the range $500\,\Omega \leq R \leq 5\,M\Omega$. Their results show that the load resistance has a significant effect on the harvested power.

Based on the model of VIVACE converter, Ding *et al.* (2013) performed two-dimensional (2-D) Unsteady Reynolds Averaged Navier-Stokes (URANS) computations to simulate the VIVACE system with two PTC-cylinders in tandem and investigate the system parameters effects on the cylinder dynamics.

Continuing their investigations on the VIVACE converter, in Ding *et al.* (2015a), the authors conducted 2-D URANS simulations to investigate the energy conversion and the behaviour of the flow around cylinders with different cross sections and for a Reynolds number varying in the range $10^4 \leq Re \leq 1.3\,10^5$. The considered cylinders have different cross sections: a circle, a square, a quasi-trapezoid and a triangle. One of their conclusions was that the circular PTC-cylinder and the quasi-trapezoid

cylinder have better efficiencies on energy harvesting comparing to the square cylinder and triangular prism. Ding *et al.* (2015b) applied 2-D URANS equations with the Spalart–Allmaras turbulence model to simulate the flow induced motions of multiple circular cylinders with passive turbulence control (PTC) in steady uniform flow. Four configurations with one, two, three, and four cylinders in tandem were simulated at Reynolds numbers in the range of $3.0\,10^4 \leq Re \leq 1.2\,10^5$. Then in Ding *et al.* (2016), two-dimensional URANS computations were performed to investigate the flow induced motion of a single and rigid circular cylinder with a pair of straight roughness strips pasted on the surface of the cylinder symmetrically with respect to the forward stagnation point.

In Ding *et al.* (2018), 2D-URANS simulations were performed in Reynolds number range of $3.0\,10^4 < Re < 1.05\,10^5$ to study the Flow-Induced Vibrations (FIV) and energy harvesting of three circular cylinders in tandem. Chizfahm *et al.* (2018) proposed VIV bladeless wind turbine (BWT) that consists of a long cylinder, flexible or mounted on a flexible structure in the flow field. The effects of the wind speed on the induced lift force, turbine deflection, and the generated power were investigated for four BWTs, two of which were long, right and conic flexible cylinder and the other two were mounted on a flexible structure. Their results showed that the conic BWTs had a higher performance at high wind speeds whereas the right circular cylinder BWTs exhibited a better performance at low wind speeds. It was also shown that more power was transmitted to the BWT when the bluff body was mounted on a flexible structure, in comparison with using a flexible bluff body. In order to estimate the energy harnessing of a square cylinder in a water flow, Zhang *et al.* (2018) carried out numerical simulations using the CFD software FLUENT. The unsteady Navier Stokes equations were solved to predict the fluid forces, then the Newmark method was employed to solve the dynamic equation. The effect of the mass and the damping ratios on the harnessed power was investigated. Zhou and Wang (2018) analysed the energy harvesting performance of two identical cantilever-based piezoelectric VIV energy harvesters. The Lattice Boltzman method (LBM) was applied to evaluate the flow-induced force due to the incoming wind and the obtained results were verified by experiments. They found that with two cylinders in tandem, the harnessed power was significantly increased compared to that of a single cylinder. Zhu *et al.* (2018) proposed a new converter consisting on a circular cylinder with an attached free-to-rotate pentagram impeller, for harvesting renewable energy from water currents. Then numerical simulations based on the solution of two-dimensional URANS equations were performed to investigate the effect of the added impeller on the vibration response of a circular cylinder. The power harnessed by this device was evaluated. They showed that the added device induced hydrodynamic instabilities at high reduced velocity, which involved an increase of the harnessed power. Adhikari *et al.* (2020) developed a mathematical model for the

analysis of piezoelectric VIV energy harvesting devices operating in random flow fields. Gu *et al.* (2019) analysed the effect of the cylinder depth on the harnessed power of an oscillating circular cylinder. They carried out numerical computations based on 2-D Navier Stokes equations coupled to the dynamic equation of the vibrating cylinder. This study was performed for Reynolds numbers in the range $1.61\,10^4 \leq Re \leq 1.05\,10^5$. They found that the harvested energy increased with the submergence depth and when the submergence depth reached a certain value, its effects became weak. The authors did not mention it but this limit value was probably a function of the diameter of the cylinder. It was also shown that for all the cases, the hydrokinetic energy conversion efficiency increases with the increasing flow speed.

Lee *et al.* (2019) considered a mechanism that consisted of a piezoelectric micro-electromechanical device excited by an oscillating cylinder subjected to air flow. Instead of using only two cylinders the authors proposed to use larger formations of up to 25 cylinders. They found that the L/D ratio had a critical role in determining the formation effect.

Zhang *et al.* (2019) investigated the effect of the angle of attack (AoA) of the incoming water flow on the energy converted by two circular cylinders in side-by-side arrangement. Two-dimensional URANS simulations were performed for Reynolds number in the range 10^3 to 10^4. The AoA of the incoming free flow was varied from 0° to 90°. They concluded that the optimum region for hydrokinetic energy conversion was $0° \leq AoA \leq 30°$ and $5\,10^3 \leq Re \leq 7\,10^3$. Recently, Shi *et al.* (2021) presented a vortex-induced vibration (VIV)-based piezoelectric energy harvester with a circular cylinder mounted on an orthogonal bi-beam system. The proposed device was tested in wind tunnel. The experiments results showed that the bi-beam wind energy harvesting exhibited high output energy and a wide range of effectively working speed for all wind directions.

A semi empirical model for aerodynamic forces was employed by Zhang *et al.* (2021b) to predict the harvested energy of a VIV circular cylinder for different Re. The model is mainly related to the amplitude-dependent aerodynamic damping parameter, where good agreement was shown between the described model and the experimental results in term of vibrations' amplitudes and average harvested power. It has been concluded that the harvested power increases proportionally with the increase of Reynolds number, although the effect of Re decreases when the mechanical damping ratio increases. A new configuration was given by Wang *et al.* (2022) to the mechanism described by Zhang *et al.* (2021b), consisted in inclining the cylinder from the vertical axis by a certain angle. The inclination enhanced significantly the vortex-induced vibration and the power generation following the combination of the torsional and the transverse vibrations. A CFD investigation, based on the Latice-Boltzman method, was performed in order to give a better understanding of the fluid flow phenomena over the vibrating cylinder.

Zhang *et al.* (2021a) carried out a numerical investigation of a laminar fluid flow over a 1 DoF circular cylinder, connected to a splitter plate at its back stagnation point; the ALE formulation of Navier Stokes equations was coupled to the motion equation of the cylinder-plate configuration. The results showed that the torsional amplitude has significant values when the reduced velocity is lower than a critical value (10), over this value, the assembly cylinder-plate oscillated in a nonzero equilibrium angle and a decrease in the oscillations amplitude was detected. The authors recommended the prescribed configuration for energy harvesting according to the high amplitude (12°) observed at a reduced velocity of 4.75.

Flapping airfoils were also considered for energy extraction. Boudis *et al.* (2018) introduced a new airfoil shape based on a combination between the *NACA* 0006 and the *NACA* 0012 airfoils to improve the energy extraction efficiency by the combined airfoil undergoing a forced flapping motion.

For a larger overview on the different energy harvesting devices designed according to the vibration-to-electricity conversion mechanisms, their representative mathematical models and the efficiency derivation methods, readers can refer to the reviews on aeroelestic energy harvesting given by Abdelkefi (2016), Rostami and Armandei (2017) and Wei and Jing (2017).

This survey shows that research is always carried out to analyse or improve the performance of energy recovery devices. There are therefore still challenges to overcome in this area. Thereby in this paper, an energy harvester device based on a water flow-induced oscillating cylinder is investigated to further improve the efficiency of such devices. To this end, the circular cylinder surface is modified by introducing new kind of PCT that consists on slots located on the front surface of the cylinder. To the authors knowledge, in all previous studies, harnessed power was improved by adding straight strips on the front surface of the cylinder. It is shown here that two slots located on the front surface of the cylinder can improve the harnessed power. To study the effect of these new kinds of PTC on the power harnessing, numerical simulations are first performed to predict the cylinder dynamic behaviour. These computations are based on the solution of the URANS equations coupled to the dynamic equations of the cylinder. Thereafter, the expected electrical power is calculated according to the cylinder displacement.

The paper is organized as follows: in the next section, the proposed new cylinder configuration is presented. Then, in section 3, the applied mathematical approach is described. The numerical model and validation study are given in section 4. Afterward, the obtained results for the new VIV harvester are discussed in section 5.

## 2. THE PROPOSED CYLINDER'S MODIFICATIONS

The device considered in this study is depicted in Fig. 1. It consists of an oscillatory circular cylinder of diameter D and mass m, mounted on a linear spring of stiffness k with a damping c. To enhance the hydrokinetic energy conversion to mechanical energy, passive turbulence control (PTC) is placed on the cylinder surface.
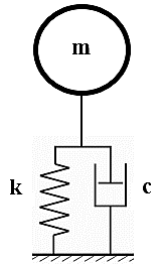
Fig. 1. Linear oscillator system: mass-spring-damper.

The baseline cylinder ($config. 0$) is analogous to that considered by Ding *et al*. (2015) which placed two straight strips at an angle $\theta = \pm28°$ from the front stagnation point. The width of each strip is $\delta_1 = 0.0127m$ and their height is $\delta_2 = 0.847\,10^{-3}m$ (Fig. 2a).

In the proposed new cylinder configuration ($config. 1$), the cylinder is provided with two slots instead of two straight strips (Fig. 2b). The width and depth of the slots are equal to the width (δ_1) and height (δ_2) of the baseline cylinder, respectively.
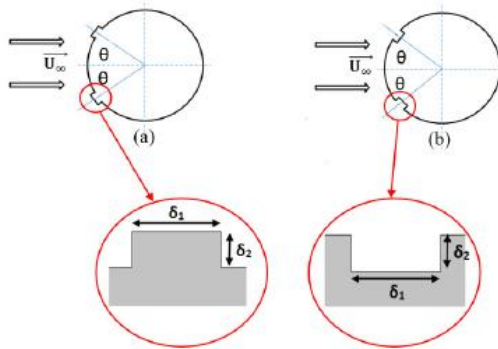
Fig. 2. Two cylinder configurations: (a) config. 0, (b) config. 1.

To predict the harvested energy from the vibrating body, it is necessary to consider the dynamic equations of the cylinder for identifying the parameters that depict the vibrating motion which are: the amplitude and the frequency.

3. MATHEMATICAL MODEL

A free cylinder in a fluid flow experiences fluctuating loads induced by the fluid. This results in an aeroelastic behavior depending on the degree of freedom (DoF) of the cylinder. The numerical study of such phenomenon involves the use of a fluid-structure interaction (FSI) technique, where the fluid and solid equations are solved in a coupled approach.

3.1 The fluid equations

The fluid flow is governed by the incompressible Unsteady Reynolds Averaged Navier-Stokes (URANS) equations. Their resolution in Fluid-Structure Interaction approach requires a dynamic mesh. The fluid equations are then written in ALE (Arbitrary Lagrangian Eulerian) coordinates.

The turbulence is modeled by the $SST\ k - \omega$ model of Menter (Menter 1994). In this model, the $K - \omega$ model is applied in the near wall zone and the standard $K - \epsilon$ model is applied in areas far from the wall.

3.2 Dynamic equations of the cylinder

Assuming that the vibrations are induced by the lift force only, however the cylinder oscillates in the vertical direction (Fig. 1). These motions are modelled by the second order linear equation derived from the Lagrange equations:

$$m\ddot{y}(t) + c\dot{y}(t) + ky(t) = F(t) \qquad (1)$$

where y is the vertical displacement of the cylinder, $\ddot{y}$ and $\dot{y}$ are the cylinder acceleration and velocity respectively and $F(t)$ is the fluid force, that is given by the equation:

$$F(t) = \frac{1}{2}\rho C_L U_\infty^2 D \qquad (2)$$

with C_L is the lift coefficient and U_∞ is the fluid velocity.

$F(t)$ is derived from the solution of the equations that govern the fluid flow.

3.3 Coupled approach

In the coupled technique applied to compute the fluid force and the cylinder displacements, the governing fluid flow equations are first solved at a time t_1, for a given cylinder position y_1. The resulting fluid force $F(t_1)$ is derived from the CFD computations and the Newmark algorithm is applied to solve the dynamic equation (Eq. (1)). The new cylinder position $y^{new} = y_1 + \delta y$ is then determined. Next, the mesh undergoes a displacement according to δy and a remeshing technique is applied to the computational grid. The fluid equations are solved at the next time step in the new computational mesh, for the new cylinder position. This process is repeated for the following time steps, during all simulated oscillation periods. A more detailed description of this approach and the applied remeshing technique can be found in Bekhti *et al*. (2016) or Guerri *et al*. (2008).

3.4 Computation of the harnessed energy

The mechanical power harvested from the vibrating body during one oscillation cycle of period T is

expressed as (Barrero-Gil *et al.* 2012, Ding *et al.* 2015):

$$P_m = \frac{1}{T} \int_0^T F \ \dot{y} \ dy \tag{3}$$

According to Eqs. (1) and (3), the harvested power writes as:

$$P_m = \frac{1}{T} \int_0^T \big(m\ddot{y}(t) + c\dot{y}(t) + ky(t) \big) \ \dot{y}dt \tag{4}$$

It is assumed that the cylinder response undergoes sinusoidal oscillations:

$$y(t) = A \ sin(2\pi f \ t) \tag{5}$$

where A is the vibration amplitude and f represents the vibration frequency.

The equation (4) is then simplified as follows:

$$P_m = \frac{1}{T} \int_0^T c \ [A \ 2\pi f \ cos(2\pi f \ t)]^2 dt \tag{6}$$

where c is the sum of the damping coefficient for the harnessing energy c_h and the damping coefficient for the dissipated energy c_d. After integration, the harvested mechanical power can be written as (Ding *et al.* 2015):

$$P_m = 8\pi^3 m\zeta f_{nw} A^2 f^2 \tag{7}$$

where ζ is the damping ratio:

$$\zeta = \frac{c}{2\sqrt{mk}} \tag{8}$$

and f_{nw} is the natural frequency in water:

$$f_{nw} = \frac{1}{2\pi} \sqrt{\frac{k}{m+m_a}} \tag{9}$$

m_a being the added mass. Finally, the harnessed power writes as:

$$P_h = \frac{c_h}{c} P_m \tag{10}$$

4. NUMERICAL MODEL

The present study is carried out using the CFD open source $Code\_Saturne$ (Archambeau *et al.* 2004), based on a cell centered finite volume method.

4.1 Algorithms and schemes

The coupled velocity-pressure equations are solved using a fractional step technique based on a prediction-correction steps (EDF R&D 2015). The Rhie and Chow filter (Rhie and Chow 1983) is used to stabilize the pressure oscillations. The Second Order Linear Upwind (SOLU) convection scheme is used for the spatial discretization. The $\theta - scheme$ is employed for the time discretization.

4.2 Computational domain and boundary conditions

A two-dimensionnal rectangular computational domain is considered. The circular cylinder is set at a distance of $15 \ D$ from the left boundary, the right boundary is located at $60 \ D$ downstream the cylinder, while the top and bottom boundaries are at $15 \ D$ from the cylinder horizontal axis. These domain's dimensions are chosen so that the free-stream fluid flow conditions are achieved at all external boundaries.

The computational domain is meshed using structured computational grid (Fig. 3).

$Inflow$ and $Outflow$ conditions are set at the left and right boundary, respectively. A $Symmetry$ condition is defined on top and bottom boundaries. The $Wall$ condition is defined at the cylinder surface.

4.3 Grid and time-step independence study

Preliminary simulations were first conducted to ensure the mesh independency on the solution. For this purpose simulations are carried out for a fixed smooth circular cylinder, where different meshes are considered: from coarse (mesh 1) with 40 elements to fine (mesh 5) with 400 elements evenly distributed over the cylinder perimeter. Calculations were performed for a Reynolds number: $Re = 10^5$, the computed drag coefficients corresponding to each mesh are presented in Table 1.

It is shown that the results are significantly improved from mesh 1 to mesh 3 (with 200 elements on the cylinder perimeter), whereas the relative error in drag coefficient decreases to less than 1% from mesh 3 to finer meshes, however the medium mesh (mesh 3) is considered for the simulation.

A two-velocity scale wall function is employed, which involves a near-wall grid spacing Δy corresponding to a dimensionless wall distance $35 \le y^+ \le 80$.
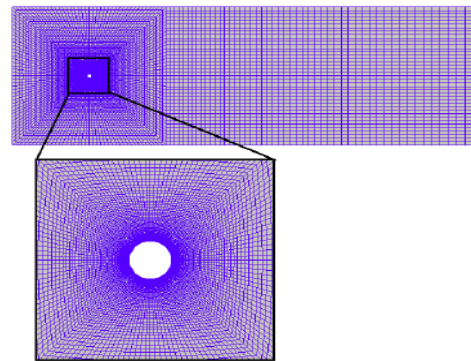

Fig. 3. Computational domain.

Table 1. Mesh independency study

	Total elements	C_D	% ΔC_D
Mesh 1	8700	1.092	-
Mesh 2	26100	1.063	2.72%
Mesh 3	43500	1.048	1.43%
Mesh 4	69600	1.043	0.47%
Mesh 5	87000	1.042	0.09%

Different time-steps are tested for an elastically mounted cylinder (Δt= 0.01 s, 0.005 s, 0.001 s, 0.0005 s and 0.0001 s) at Re=8 10^4. Results stability is obtained at Δt=0.0005s.

This time step corresponds to the time spent by a fluid particle across a half of cell:

$$\Delta t \approx \frac{U_\infty \times D}{2 \times N} \qquad (11)$$

Where N=100 is the number of elements on the cylinder half perimeter.

Therefore, the time step Δt=0.0005 s is considered for Re=8 10^4.

As the velocity is inversely proportional to the time, the time step decreases when the Re increases, however the time step Δt_i corresponding to the other cases of Re_i is calculated according to the following formula:

$$\begin{cases} \Delta t_i = \frac{Re_i - 10^4}{Re_i} \Delta t_{i-1} \\ Re = 8 \ 10^4 \rightarrow \ \Delta t = 0.0005 \end{cases} \qquad (12)$$

and then Δt is simplified and minimized by deleting the digits lower than 10^{-4}.

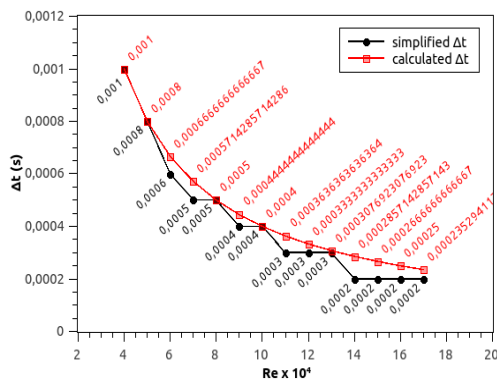In Fig. 4 are presented the time steps corresponding to each Re.

Fig. 4. Time step variation with Re.

These values validate the following condition:

$$\frac{U_\infty \times \Delta t}{\Delta h} < 1 \qquad (13)$$

where Δh=0.001m is the thickness of the first cells row on the cylinder.

5. RESULTS AND DISCUSSION

A validation study is first performed for an elastically mounted cylinder oscillating in a water flow. Then the cylinder with the proposed new PTC configuration is considered.

5.1 Validation study

The baseline cylinder configuration ($config. 0$) is considered for the validation study.

In order to compare our numerical results with published data, the calculation parameters are chosen

accordingly to that used by Chang (2010), Ding *et al.* (2013) and Ding *et al.* (2015). The mechanical and physical parameters of the oscillating system and water are summarized in Table 2.

Table 2. Mechanical and physical parameters of the oscillating system and water

Cylinder diameter D	0.0889 m
Mass m	11.76 kg
The added mass m_a	6.2 kg
Damping coefficient of the oscillating system c	14.97 Ns/m
Damping coefficient for energy harnessing c_h	11.47 Ns/m
Stiffness k	1750 N/m
Density of water ρ	999.1026 kg/m^3
Kinematic viscosity of water ν	1.139 10^{-6} m^2/s

The vertical displacements of the cylinder are depicted in Fig. 5 which shows that the trajectory follows a sinusoidal motion with an amplitude and frequency varying with the Reynolds number Re.

The dimensionless amplitudes $(A^* = A/D)$ are depicted in Fig. 6 for Reynolds number varying from 4. 10^4 to 12. 10^4.

The present numerical model induces a delay of the transition region preceding the galloping phase; however, the transition region takes place at $10 \ 10^4 < Re < 11 \ 10^4$.

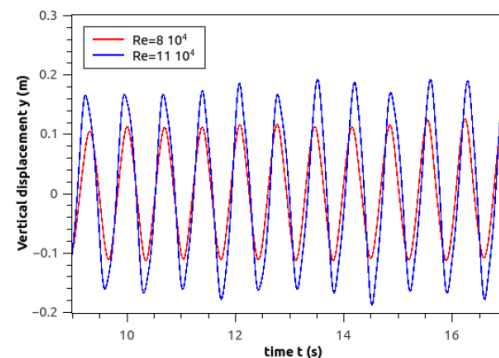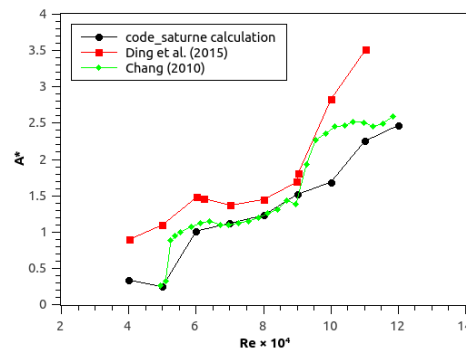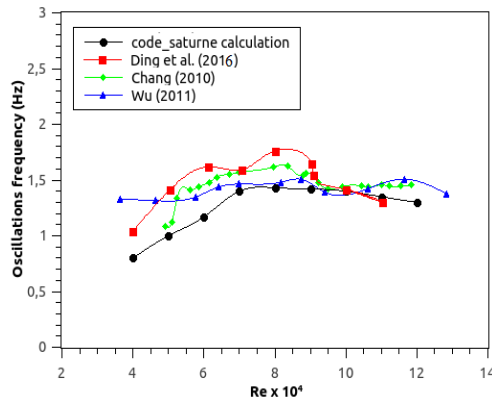**Fig. 5. Cylinder vertical displacement for Re = 8. 10^4 and Re = 11. 10^4.**

Fig. 6. Amplitude of the baseline cylinder (config.0) for different Reynolds numbers.

Fig. 7. Frequency of the PTC cylinder for different Re.

Fig. 8. Amplitude variation with Re.

These results are broadly consistent with the experimental data presented by Chang (2010). Thus, we can consider that the flow induced vibration phenomenon is well predicted by the present model.

Figure 7 shows the vibrations frequencies for different Reynolds number. Results of the present study are compared to published experimental studies (Chang 2010, Wu 2011 and Ding *et al.* 2016); the evolution pace is achieved and good agreement is obtained for Re > 7 10^4.

The effects of the proposed new PTC configuration on the harvested power are then investigated. These computations are performed for Reynolds numbers in the range: $4\ 10^4 \leq Re \leq 17\ 10^4$.

5.2 Effect of the new configuration on the cylinder's vibration amplitudes

The variations of the dimensionless amplitude versus the Reynolds number is depicted in Fig. 8 for the proposed cylinder configuration ($config.1$), compared to the baseline configuration ($config.0$).

These results show that largest amplitudes are achieved with the new configuration, compared to $config.0$. It appears that the slots of the proposed configuration ($config.1$) conduct to increase the oscillations amplitude. This is due to the higher flow-induced forces caused by the slots given to *config.1*.

According to Ding *et al.* (2016), the galloping is initiated for Re > $10\ 10^4$ and it is related to the geometry of the vibrating object, where the asymmetry boosts the increase of the oscillations amplitude. Due to the fully developed instability at high Reynolds, shortcomings in numerical resolution could occur at Re=$14\ 10^4$ and $16\ 10^4$ where the amplitude undergoes a dramatic drop.

The smooth cylinder oscillations undergo an abrupt dump at Re=$9\ 10^4$. At this stage, the de-synchronization mode takes place which traduced by a dramatic decrease of the vibrations' amplitude.

5.3 Vortex pattern

Computations are carried out beforehand for a fixed cylinder, then for an oscillating cylinder, to characterize the vortex shedding. A comparison
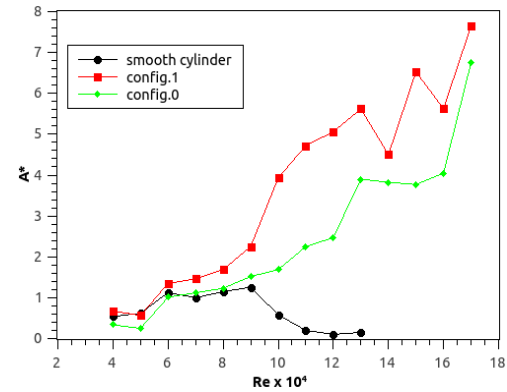
between the baseline cylinder configuration and $config.1$ is presented.

5.3.1 Vortex shedding from a fixed cylinder

The vortex patterns around a fixed cylinder are depicted in Fig. 9 for $Re = 7.10^4$, 13.10^4, and 17.10^4. It can be seen that with the two slots of the $config.1$ cylinder, the flow detachment and the position of the vortices shedding (x_{shed}) are shifted towards the leading edge; which leads to increase the intensity of the vorticity downstream the cylinder.

5.3.2 Case of the oscillating cylinders

Figures 10 to 12 show the wake patterns of a vibrating cylinder at times $t = T/4, T/2, 3T/4$, and T, for Reynolds numbers $Re = 8.10^4$, 11.10^4, and 16.10^4. For the lower Reynolds, the vortices are slightly affected by the cylinder motion for both $config.0$ and $config.1$. By increasing Re, the vortex shedding frequency increases and generates high-intensity vortices, which leads to the vortex-induced vibration phenomenon with higher amplitudes. In these cases, it should be noted that the fluid velocity acting on the cylinder is the resultant of the far field flow velocity and the cylinder displacement velocity. For all studied cases, the oscillation frequency varies between $1.25\ Hz$ to $1.49\ Hz$, which is lower than the natural frequency in water $f_{nw} = 1.57\ Hz$.

5.4 Hydro-kinetic energy conversion

The methodology presented in section 3.4 is applied to evaluate the expected harnessed power. The harvested and the harnessed power variation versus Re are depicted in Fig. 13.

For $Re \leq 9\ 10^4$, the harnessed power increases weakly with Re, while a steep increase in power is noticed for $Re > 9\ 10^4$.

The figure 14 shows the difference between the harnessed power from both $config.0$ and $config.1$ ($\Delta P = P_{h.config.1} - P_{h.config.0}$).

The gain in power ΔP is significant when using the new PTC configuration for the Reynolds numbers in the range: $9.10^4 \leq Re \leq 16.10^4$, where the maximum value is registered for $Re = 15.10^4$.

(a) Re=7 10^4

(b) Re=13 10^4

(c) Re=17 10^4
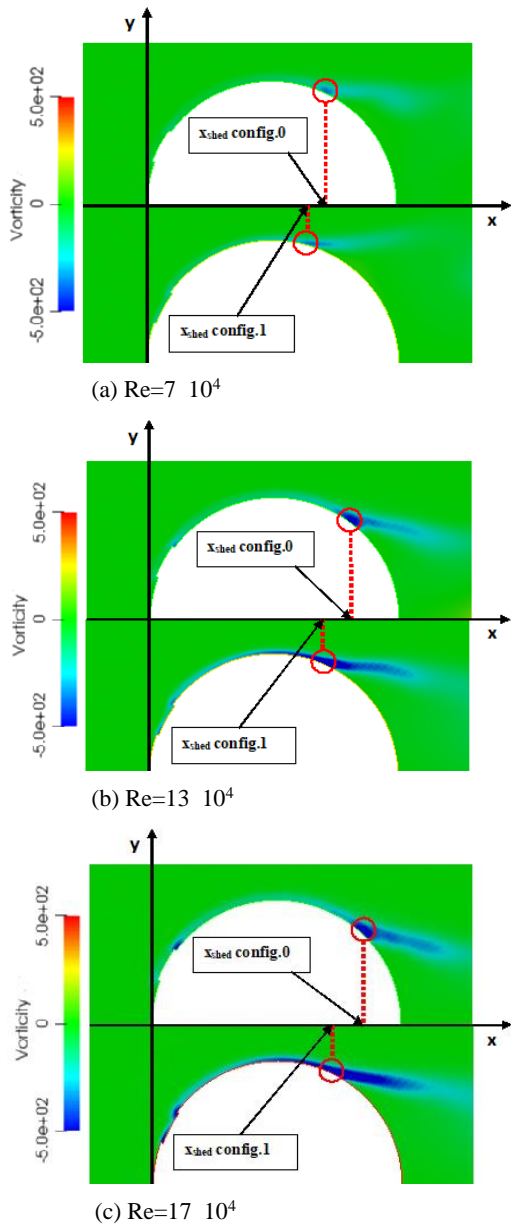
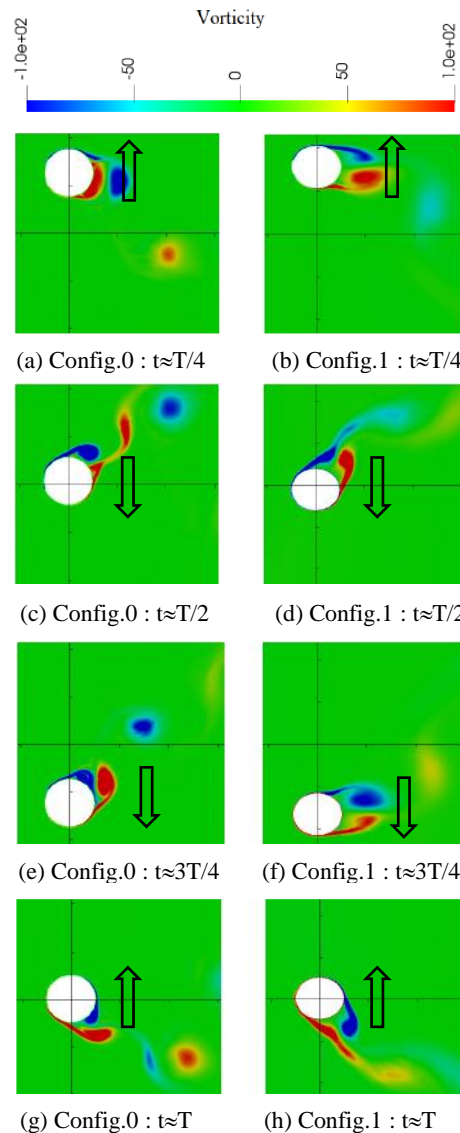**Fig. 9. Vortex shedding from a fixed cylinder different Reynolds numbers.**

As reported in the section 5.2, the shifted flow detachment caused by the two slots in $config.1$ induces vibrations with high amplitudes, which can conduct to reach the hydrodynamic instability, however it can be drawn that $config.1$ allows to reduce the vibrations damping effect.

Figure 15 shows the power improvement rate τ for a series of Re while using the $config.1$.

The maximum rate of the harnessed power improvement is obtained for $Re = 10\ 10^4$.

Due the galloping mode, the converted power undergoes a sharp increase at Re=13 10^4, followed by a an abrupt drop at Re=14 10^4 (Fig. 13) caused by the drop of the oscillations amplitude seen in section 5.1; whereas at Re=15 10^4, the converted

power curve resumes its increasing evolution; however, important differences between the converted powers at Re=13 10^4/15 10^4 and Re=14 10^4 are shown in Fig. 14.

(a) Config.0 : t≈T/4   (b) Config.1 : t≈T/4

(c) Config.0 : t≈T/2   (d) Config.1 : t≈T/2

(e) Config.0 : t≈3T/4   (f) Config.1 : t≈3T/4
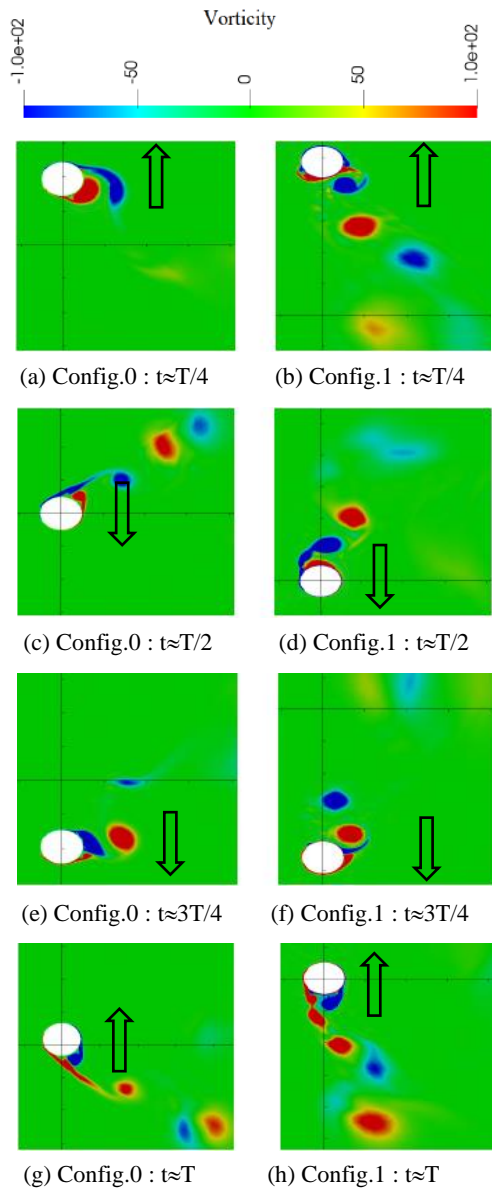
(g) Config.0 : t≈T   (h) Config.1 : t≈T

Fig. 10. Vortex shedding for Re = 8 10^4.

6. CONCLUSION

The harnessed power from Flow-Induced Vibrations of a new modified circular cylinder is considered in the present paper. The proposed cylinder modification consists in adding two slots located at an angle of $\pm16°$ from the leading edge, instead of two straight strips.

A numerical model based on the coupling of the fluid equations with the solid dynamic equations is applied to predict the cylinder behaviour in a turbulent flow. Thereafter, the harvested and harnessed power are calculated.

(a) Config.0 : t≈T/4   (b) Config.1 : t≈T/4

(c) Config.0 : t≈T/2   (d) Config.1 : t≈T/2

(e) Config.0 : t≈3T/4   (f) Config.1 : t≈3T/4

(g) Config.0 : t≈T   (h) Config.1 : t≈T
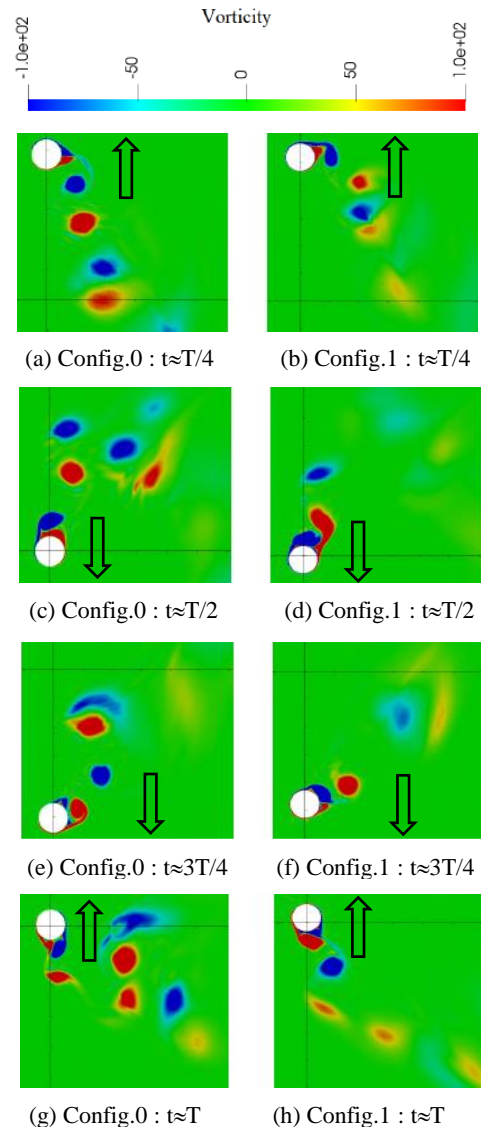
Fig. 11. Vortex shedding for Re = 11 10⁴

First, in a validation study, it is shown that the results obtained with the applied numerical model are in good agreement with published experimental Data. The investigations performed on the proposed new modified cylinder show that the slots lead to move the flow detachment point toward the leading edge.

This involves higher hydrodynamic instabilities resulting in higher oscillations amplitudes, and thereby, a significant enhancement of the harnessed power is found; the maximum rate of the power improvement ($\tau \approx 320\%$) corresponds to a Reynolds number of $10 \ 10^4$.
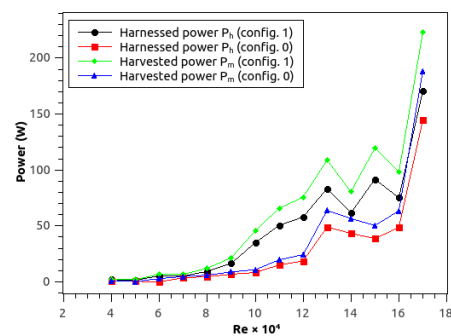
For further improvements of the VIV harnessed power, next investigations should be performed for a series of cylinders where the effect of the cylinder spacing and slot positions on the total harnessed power should be considered.

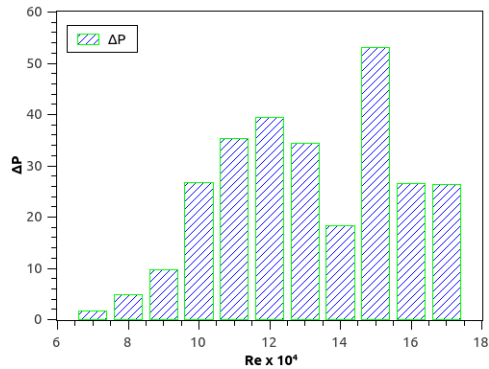(a) Config.0 : t≈T/4   (b) Config.1 : t≈T/4

(c) Config.0 : t≈T/2   (d) Config.1 : t≈T/2

(e) Config.0 : t≈3T/4   (f) Config.1 : t≈3T/4

(g) Config.0 : t≈T   (h) Config.1 : t≈T

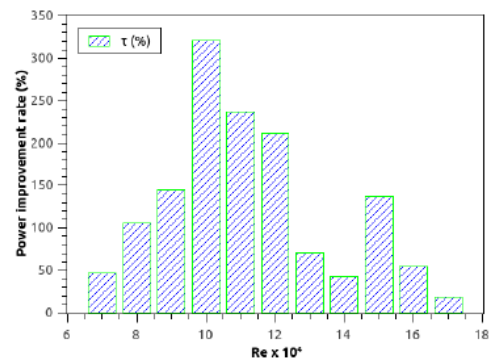**Fig. 12. Vortex shedding for Re = 16 10⁴.**

Fig. 13. Harnessed power variations with Re.

Fig. 14. Power difference between config.0 and config. 1.

Fig. 15. Harnessed power improvement rate.

REFERENCES

Abdelkefi, A. (2016). Aeroelastic energy harvesting: A review. *International Journal of Engineering Science* 100, 112–135.

Adhikari, S., A. Rastogi and B. Bhattacharya (2020). Piezoelectric vortex induced vibration energy harvesting in a random flow field. *Smart Materials and Structures* 29(3), 035034.

Archambeau, F., N. Mechitoua and M. Sakiz (2004). Code saturne: A finite volume code for the computation of turbulent incompressible flows. *International Journal on Finite Volumes* 1, 1–62.

Barrero-Gil, A., S. Pindado and S. Avila (2012). Extracting energy from vortex-induced vibrations: a parametric study. *Applied Mathematical Modelling* 36, 3153–3160.

Bekhti, A., O. Guerri and T. Rezoug (2016). Flap/lead-lag computational investigations on NREL S809 airfoil. *Mechanics & Industry* 17(6), P606.

Bernitsas, M. M. and K. Raghavan (2005). Fluid motion energy converter. International. Provisional Patent Application, USA Patent and Trademark Office.

Bernitsas, M. M., K. Raghavan, Y. Ben-Simon and E. M. H. Garcia (2006). VIVACE (Vortex Induced Vibration Aquatic Clean Energy): a new concept in generation of clean and renewable energy from fluid flow. *Journal of Offshore Mechanics and Arctic Engineering* 130.

Boudis, A., A. Benzaoui, H. Oualli, O. Guerri, A. C. Bayeul-Lain´e and O. C. Delgosha (2018). Energy extraction performance improvement of a flapping foil by the use of combined foil. *Journal of Applied Fluid Mechanics* 11(6), 1651–1663.

Chang, C. C. (2010). Hydrokinetic energy harnessing by enhancement of flow induced motion using passive turbulence control. Ph. D. thesis, Naval architecture and marine engineering. Ann Arbor: University of Michigan.

Chang, C. C. J., R. A. Kumar and M. M. Bernitsas (2011). VIV and galloping of single circular cylinder with surface roughness at $3.0{\times}10^4{\leq}Re{\leq}1.2{\times}10^5$. *Ocean Engineering* 38, 1713–1732.

Chizfahm, A., E. A. Yazdi and M. Eghtesad (2018). Dynamic modeling of vortex in duced vibration wind turbines. *Renewable Energy* 121, 632–643.

Ding, L., L. Zhang, C. Wua, X. Maoa and D. Jiang (2015a). Flow induced motion and energy harvesting of bluff bodies with different cross sections. *Energy Conversion and Management* 91, 416–426.

Ding, L., L. Zhang, E. S. Kim and M. M. Bernitsas (2015b). 2-D URANS vs. experiments of flow induced motions of multiple circular cylinders with passive turbulence control for 30,000<Re<105,000. *Journal of Fluids and Structures* 54, 612–628.

Ding, L., L. Zhang, M. M. Bernitsas and C. C. Chang (2016). Numerical simulation and experimental validation for energy harvesting of single-cylinder VIVACE converter with passive turbulence control. *Renewable Energy* 85, 1246–1259.

Ding, L., M. M. Bernitsas and E. S. Kim (2013). 2-D URANS vs. experiments of flow induced motions of two circular cylinders in tandem with passive turbulence control for 30,000<Re<105,000. *Ocean Engineering* 72, 429–440.

Ding, L., Q. Zou, L. Zhang and H. Wang (2018). Research on flow-induced vibration and energy harvesting of three circular cylinders with roughness strips in tandem. *Energies* 11, 2977.

EDF R&D (2015). Code Saturne 4.0.0 Theory Guide. EDF R&D.

Gu, M., B. Song, B. Zhang, Z. Mao and W. Tian (2019). The effects of submergence depth on vortex-induced vibration (VIV) and energy harvesting of a circular cylinder. *Renewable Energy* 151, 931–945.

Guerri, O., A. Hamdouni and A. Sakout (2008). Fluid structure interaction of wind turbine airfoils. *Wind Engineering* 32(6), 539–557.

Lee, Y. J., Y. Qi, G. Zhou and K. B. Lua (2019). Vortex-induced vibration wind energy harvesting by piezoelectric MEMS device in formation. Scientific Reports 9(1), 1–11.

Mehmood, A., A. Abdelkefi, M. R. Hajj, A. H. Nayfeh, I. Akhtar and A. O. Nuhait (2013). Piezoelectric energy harvesting from vortex induced vibrations of circular cylinder. *Journal of Sound and Vibration* 332, 4656–4667.

Menter, F. R. (1994). Two-equation eddyviscosity turbulence models for engineering applications. *AIAA Journal* 32, 1598–1605.

Rhie, C. and W. Chow (1983, November). Numerical study of the turbulent flow past an airfoil with trailing edge separation. *AIAA Journal* 21(11), 1525–1532.

Rostami, A. B. and M. Armandei (2017). Renewable energy harvesting by vortex induced motions: Review and benchmarking of technologies. *Renewable and Sustainable Energy Reviews* 70, 193–214.

Shi, T., G. Hu, L. Zou, J. Song and K. C. S. Kwok (2021). Performance of an omnidirectional piezoelectric wind energy harvester. *Wind Energy* 24(1167-1179).

Wang, J., C. Zhang, D. Yurchenko, A. Abdelkefi, M. Zhang and H. Liu (2022). Usefulness of inclined circular cylinders for designing ultra-wide bandwidth piezoelectric energy harvesters: Experiments and computational investigations. *Energy* 239, 122203.

Wei, C. and X. Jing (2017). A comprehensive review on vibration energy harvesting: Modelling and realization. *Renewable and Sustainable Energy Reviews* 74, 1–18.

Wu, W. (2011). *Two-Dimensional RANS simulation of Flow Induced Motion of Circular Cylinder with Passive Turbulence Control*. Ph. D. thesis, Naval architecture and marine engineering. Ann Arbor: University of Michigan.

Xie, X. D. and Q. Wang (2015). Energy harvesting from a vehicle suspension system. *Energy* 86, 385–392.

Zhang, B., Z. Mao, B. Song, W. Ding and W. Tian (2018). Numerical investigation on effect of damping-ratio and mass-ratio on energy harnessing of a square cylinder in FIM. *Energy* 144, 218–231.

Zhang, L., X. Mao and L. Ding (2019). Influence of attack angle on vortex-induced vibration and energy harvesting of two cylinders in side-by-side arrangement. *Advances in Mechanical Engineering* 11(1), 1–13.

Zhang, M., X. Wang and O. Øiseth (2021a). Torsional vibration of a circular cylinder with an attached splitter plate in laminar flow. *Ocean Engineering* 236, 109514.

Zhang, M., C. Zhang, A. Abdelkefi, H. Yu, O. Gaidai, X. Qin, H. Zhu and J. Wang (2021b). Piezoelectric energy harvesting from vortex-induced vibration of a circular cylinder: Effect of Reynolds number. *Ocean Engineering* 235, 109378.

Zhou, S. and J. Wang (2018). Dual serial vortex induced energy harvesting system for enhanced energy harvesting. *AIP Advances* 8, 075221.

Zhu, H., Y. Zhao and T. Zhou (2018). CFD analysis of energy harvesting from flow induced vibration of a circular cylinder with an attached free-to-rotate pentagram impeller. *Applied Energy* 212, 304–321.